New Family of Argyrodite Thioantimonate Lithium Superionic Conductors

Laidong Zhou, [a] *Abdeljalil Assoud,* [a] *Qiang Zhang,* [b] *Xiaohan Wu,* [c] *Linda F. Nazar* [a]*

[a] Department of Chemistry and the Waterloo Institute for Nanotechnology, University of Waterloo, 200 University Avenue West, Waterloo, Ontario N2L 3G1, Canada

[b] Neutron Scattering Division, Oak Ridge National Laboratory, Oak Ridge, Tennessee 37830, United States

[c] BASF SE, Ludwigshafen 67056, Germany

Corresponding Author

* E-mail: lfnazar@uwaterloo.ca

Abstract

We report on a new family of argyrodite lithium superionic conductors, as solid solutions $Li_{6+x}M_xSb_{1-x}S_5I$ (M = Si, Ge, Sn), that exhibit superionic conductivity. These represent the first antimony argyrodites to date. Exploration of the series using a combination of single crystal X-ray and synchrotron/neutron powder diffraction, combined with impedance spectroscopy, reveals that an optimal degree of substitution (x), and substituent induces slight S^{2-}/I^- anion site disorder - but more importantly drives Li^+ cation site disorder. The additional, delocalized Li-ion density is located in new high energy lattice sites that provide intermediate interstitial positions (local minima) for Li^+ diffusion and activate concerted ion migration, leading to a low activation energy of 0.25 eV. Excellent room temperature ionic conductivity of 14.8 $mS{\cdot}cm^{-1}$ is exhibited for cold-pressed pellets - up to 24 $mS{\cdot}cm^{-1}$ for sintered pellets (owing to better grain boundary contact) - amongst the highest values reported to date. This enables all-solid state battery prototypes that exhibit promising properties. Furthermore, even at -78 °C, suitable bulk ionic conductivity of the electrolyte is retained (0.25 $mS{\cdot}cm^{-1}$). Selected thioantimonate iodides demonstrate good compatibility with Li metal, sustaining over 1000 hours of Li stripping/plating at current densities up to 0.6 $mA{\cdot}cm^{-2}$. The significantly enhanced Li ion conduction and lowered activation energy barrier with increasing site disorder reveals an important strategy toward the development of superionic conductors.

Introduction

All-solid-state batteries (ASSBs) offer the promise of safe next-generation high energy density storage systems by using a solid electrolyte and (ideally) a lithium metal anode.[1,2] Highly ionically conductive solid-state electrolytes (SSEs) (> 1 $mS \cdot cm^{-1}$) are the key component which remove the safety concerns inherent with flammable organic liquid electrolytes in Li-ion batteries. To realize the potential of ASSBs, a range of new SSE materials have been developed and investigated, including oxides, phosphates, thiophosphates (sulfides), halides, and metal-organic framework/covalent organic frameworks.[3-11] Of these choices, sulfide SSEs generally exhibit high ionic conductivity (σ_i) along with a ductile nature that makes them relatively easy to process, and thus have been a particular focus of research.[12] There have also been many studies on interfacial reactions between SSEs and either cathodes or anodes,[13-20] cathode material/Li anode coatings,[21-26] and the problem of volume change.[27] Most ASSBs reported in the literature can only be cycled at low current density with low active material loading, as they are limited by moderate ionic conductivity of the SSEs and/or poor contact between the SSEs and active materials. Ultra-highly conductive (>10 $mS \cdot cm^{-1}$) and relatively soft SSEs offer the possibility to achieve high energy densities with improved rate capabilities, which are enabled by utilizing thick electrode configurations and a high active cathode material loading.[28]

Until now, only a limited number of SSEs have been reported with conductivity approaching 10 $mS \cdot cm^{-1}$; namely $Li_{10}GeP_2S_{12}$ and related phases with substitution of the Ge for Si and Sn[29,30,31], $Li_7P_3S_{11}$[32], and Ge-substituted Li-argryodite.[33] Most of these materials exhibit high σ_i (>10 $mS \cdot cm^{-1}$) for pellets sintered at elevated temperatures, but much lower σ_i for "cold-pressed" pellets prepared at ambient temperature due to poorer crystallite contact (**Table 1**). While sintered values are more indicative of the inherent bulk conductivity, practical ASSBs require their electrode/electrolyte components to be pressed at ambient temperature to limit reactivity. Classic argyrodites Li_6PS_5X (X=Cl, Br) [34,35] have attracted considerable interest, due to their good σ_i (up to 4 - 5 $mS \cdot cm^{-1}$ by direct annealing of precursors, [36] or from scalable solution-engineered synthesis[37]). The σ_i of argyrodites is strongly dependent on the S^{2-}/X^- (X=Cl, Br, I) disorder over the 4*a* and 4*c* sites as demonstrated by density functional theory molecular dynamics simulations (DFT MD).[38] Indeed, Cl/Br compositions with mixed halide occupation on these sites give rise to higher σ_i (up to 4 $mS \cdot cm^{-1}$) than either pure Cl or Br compositions.[37,42] As Li_6PS_5I exhibits no

Table 1. Comparison of ionic conductivities between cold pressed powders and sintered pellets for some recently reported superionic conductors.

Compositions	Cold-pressed powder ($mS \cdot cm^{-1}$)	Ref.	Sintered Pellet ($mS \cdot cm^{-1}$)	Ref.
$Li_7P_3S_{11}$	3.2	32	17 (hot-pressing)	32
$Li_{10}GeP_2S_{12}$	5-9	21, 39	12	29
$Li_{10.35}Sn_{0.27}Si_{1.08}P_{1.65}S_{12}$	3.31	30	11	30
$Li_{9.54}Si_{1.74}P_{1.44}S_{11.7}Cl_{0.3}$	3-16	40, 41	25	31
$Li_{6.6}Ge_{0.6}P_{0.4}S_5I$	5.4	33	18.4	33
$Li_{6.7}Si_{0.7}Sb_{0.3}S_5I$	12.6	This work	19	This work
$Li_{6.6}Si_{0.6}Sb_{0.4}S_5I$	14.8	This work	24	This work

S^{2-}/I^- disorder due to the large ionic radii difference between S^{2-} and I^-,[42] this arrangement leads to very low σ_I, in the range of 1.3 $x10^{-3}$ $mS \cdot cm^{-1}$.[42] Recently, Zeier's group reported Ge-substituted Li_6PS_5I phases.[33] As the Ge content increases from 0 to 0.6, a small degree (*ca*. ~7%) of S^{2-}/I^- site disorder is induced based on powder X-ray and neutron diffraction analysis, which was correlated to a drop in the activation energy and a dramatic increase in σ_i. The composition $Li_{6.6}P_{0.4}Ge_{0.6}S_5I$ exhibits a high σ_i of 5.4 $mS \cdot cm^{-1}$ for the cold pressed material, and triple that for the sintered pellet (see **Table 1**). However, whether the induced S^{2-}/I^- disorder is due to a larger unit cell upon Ge^{4+} substitution, which allows for better mixing of the mismatched anions, or owes to the increased Li^+ concentration in the structure was not identified in this report.[33,43]

Here, we report on a new family of thioantimonate iodide argyrodites $Li_{6+x}M_xSb_{1-x}S_5I$ (M=Si, Ge, Sn), where the highest ionic conductivities above 10 $mS \cdot cm^{-1}$ are exhibited by Si compositions ($0.5 \leq x \leq 0.7$) that constitute low-cost, abundant elements. They are prepared *via* simple, non-ball milled synthesis. Optimum values were obtained for x = 0.6 (σ_i = 14.8 $mS \cdot cm^{-1}$, cold pressed pellet; σ_i = 24 $mS \cdot cm^{-1}$, sintered pellet, see **Table 1**). These materials demonstrate good compatibility with Li metal, sustaining over 1000 hours of stripping/plating at current densities up to 0.6 $mA \cdot cm^{-2}$, and enable good room temperature cycling performance in prototype ASSBs. Moreover, with the aim to unravel the underlying factors driving the superionic conductivity, a combination of exact structure solution enabled by single crystal X-ray and powder X-ray synchrotron/neutron methods reveal the origin of the fundamental structural changes associated with increased Li^+ content and anion/cation site disorder. Highly delocalized lithium ion density in the lattice serves as important interstitial sites for Li^+ diffusion and activate concerted ion migration, leading to a lowering of the activation energy from 0.41 eV to 0.25 eV. We find

that Li^+ ion disorder and concentration dictate superionic conductivity more so than anion site disorder, although the two factors are not necessarily independent.

Experimental methods

Materials synthesis

A simple approach based on mixing and heating of the precursors was used. Stoichiometric amounts of Li_2S (99.98%), P_2S_5 (99%), Sb_2S_3 (99.995%), Si (99%), GeS_2 (Kojundo, 99.99%), SnS_2 (Kojundo, >99.9%), S (99.98%) and LiI (99.9%) (the source was Sigma-Aldrich unless otherwise stated) were mixed together in an agate mortar at the targeted ratio, and 5 wt% excess sulfur was added to fully oxidize Si and Sb_2S_3. The mixtures were pelletized and placed in a glassy-carbon crucible in a sealed quartz tube under vacuum. $Li_{6+x}Si_xSb_{1-x}S_5I$ was heated to 550°C ($0.5 \leq x \leq 0.7$) or 500 °C ($0.1 \leq x \leq 0.4$) for 7 days with a ramp rate of 5 °C·min^{-1} (designated as *as-synthesized* materials). To improve purity, the as-synthesized samples were ground, repelletized and heated again to 500 °C for another 7 days at a ramp rate of 5 °C·min^{-1} (designated as *annealed* materials). $Li_6Sb_xP_{1-x}S_5I$ was heated to 550°C ($0.1 \leq x \leq 0.4$) or 500 °C ($0.5 \leq x \leq 1$) for 100 h with a ramp rate 5 °C·min^{-1}. $Li_{6+x}Ge_xSb_{1-x}S_5I$ was heated to 550 °C for 50 h, then cooled down to 450 °C for another 100 h with an ramp rate of 5 °C·min^{-1}. $Li_{6+x}Sn_xSb_{1-x}S_5I$ was heated to 550 °C for 50 h with the same ramp rate. Finally, the final product in each case was gently separated to find single crystals suitable for single crystal diffraction. The remaining crystals, or those from subsequent synthesis preparations, were crushed into polycrystalline powders for X-ray and neutron diffraction and impedance spectroscopy analysis.

Single crystal diffraction and structure resolution

Several colorless plate-shaped single crystals with dimensions of approximately 0.040 × 0.040 × 0.030 mm^3 were scanned to determine their quality. Multiple data sets were collected and gave exactly the same results. The data were collected on a BRUKER KAPPA diffractometer equipped with a SMART APEX II CCD, utilizing graphite-monochromated Mo-Kα radiation. The crystals were protected by Paratone-N oil and a liquid nitrogen flow using an OXFORD Cryostream controller 700 at 280 K to ensure no reactivity of the materials occurred. The data were collected by scanning ω and ϕ of 0.3° or 0.5° in a few groups of frames at different ω and ϕ and an exposure time of 30 or 60 seconds per frame. The data were corrected for Lorentz and polarization effects. Absorption corrections were based on fitting a function to the empirical transmission surface as sampled by multiple equivalent measurements using SADABS. Cell_now

software was used for the twinned data. The structure was solved using direct methods to locate the positions of Sb/Si/Ge/Sn, S and I atoms. First, these positions were anisotropically refined using the least squares method incorporated in the SHELXTL package, and then the Li positions were located in the remaining electron density in the Fourier map, which revealed Li-S bonds very similar in length to those found in binary and ternary Li sulfides. Subsequently, the Li site occupancies were freely and anisotropically refined. The refinements were converged to good residual values R1 and wR^2. The program Tidy was used to standardize the atomic positions. No constraints were used during the structure refinements, aside from fixing the Sn/Sb occupancy to the experimental targeted value due to the similar X-ray scattering of Sn and Sb. No constraints were used for Si:Sb or Ge:Sb occupancy refinement. The Li2 (24*g*) site was only identified in $Li_{6.2}Sn_{0.2}Sb_{0.8}S_5I$ and was isotropically refined. Indexing the unit cell reflections (with I/sigma below 5) to check for a possible supercell was carried out, but no supercells with either completely or partially ordered atomic positions were found for any single crystal composition.

X-ray and neutron powder diffraction and Rietveld analysis

Powder X-ray diffraction (XRD) measurements on all materials were conducted at room temperature on a PANalytical Empyrean diffractometer with Cu-Kα radiation that was equipped with a PIXcel bidimensional detector. XRD patterns were obtained in Debye-Scherrer geometry, with samples sealed in sealed in 0.3 mm glass capillaries under argon. For Rietveld analysis of the $Li_{6+x}Si_xSb_{1-x}S_5I$ series, synchrotron XRD measurements were also carried out on the Macromolecular Crystallography Facility beamline at the Canadian Light Source (CLS). The samples were sealed in 0.5 mm glass capillaries and data was collected at wavelength of an energy 18 KeV. The patterns were refined using the Rietveld method[44] within the GSAS II software package[45] to determine the unit cell parameters, atomic positions and occupancies (aside from Li). Refinement took benefit from the significantly different X-ray scattering factors between the component elements and the well-defined peak shapes afforded by synchrotron diffraction. This data was especially essential to resolve the very low degree of S^{2-}/I^- disorder, where the mixed S^{2-}/I^- occupancy on the 4*a* and 4*c* site was refined without occupancy constraints, and the Uiso value for S^{2-} and I^- was refined to be equal at the same sites. No other constraints were used.

The time-of-flight (TOF) powder neutron diffraction patterns were collected on POWGEN at the Spallation Neutron Source (SNS) at the Oak Ridge National Laboratory. The sample (~ 2 g)

was loaded into a vanadium can under an argon atmosphere and sealed with a copper gasket and aluminum lid. The samples were measured at 300 K or 195 K, and a single bank wave with center wavelength of 1.5 Å was used. As Li possesses a negative neutron scattering length, the patterns were refined using the Rietveld method[44] in the TOPAS V6 software package (using the structural models from the synchrotron data and difference Fourier mapping) to locate the Li positions. Bond Valence Site Energy (BVSE) calculations[46] (see supporting information for detail) used neutron structural results as the input structure.

Ionic conductivity and activation energy measurements

Ionic conductivities were measured by electrochemical impedance spectroscopy (EIS) with 100 mV constant voltage in the frequency range of 1 MHz - 100 mHz using a VMP3 potentiostat/galvanostat (Bio-Logic).

For measurements on cold-pressed pellets, ~150 mg of *as-synthesized* or *annealed* sample powder was placed between two stainless steel rods in a custom-made Swagelok cell and pressed into a 10 mm diameter pellet by a hydraulic press at 3 tons for 3 min in an Ar-filled glovebox. EIS experiments were performed at 3 tons.

For measurements on sintered pellets, 250 mg of *annealed* sample powder was pressed into pellet by a hydraulic press at 3 tons, using a 10 mm pellet die. Pellets were sealed in carbon-coated quartz tubes under vacuum and heated to 500 ^{o}C for 18 h and cooled to room temperature with a ramp rate of 5 ^{o}C·min^{-1}. Two indium foils were attached to either side of the sintered pellet to ensure good contact. EIS measurements were conducted at 0.4 tons.

For activation energy measurements, ~ 300 mg *as-synthesized* powder was placed between two stainless steel rods and pressed into a 10 mm diameter pellet by a hydraulic press at 3 tons for 3 min in a custom-made Swagelok cell and then two indium foils were attached to either side of the pellet to ensure good contact. Impedance was measured from 35 MHz to 100 mHz with 100 mV constant voltage, at temperatures ranging from 30 ^{o}C to 60 ^{o}C using a MTZ-35 impedance analyzer (Bio-Logic). For low temperature impedance measurements, sealed cells were equilibrated in a dry ice/acetone bath until the temperature fully stabilized prior to impedance measurement. All equivalent circuit fits were performed using the RelaxIS software package V3.

Electrochemical measurements

For the fabrication of Li | SSE | Li symmetric cells, ~ 100 mg of $Li_{6.7}Si_{0.7}Sb_{0.3}S_5I$ or $Li_{6.4}Ge_{0.4}Sb_{0.6}S_5I$ powder was placed into a poly(ether ether ketone) (PEEK) cylinder and cold-

pressed pressed at 3 tons for 1 min (10 mm diameter). On both sides of the SSE pellet, Li foil (99.9%, Sigma-Aldrich, 0.38 mm thickness) with a diameter of 10 mm was attached. The cell was subjected to constant uniaxial pressure using the screw of a stainless steel framework with 4 Nm torque. Galvanostatic cycling of the symmetric cell for $Li_{6.7}Si_{0.7}Sb_{0.3}S_5I$ was carried out at a current density and capacity of a) 0.3 $mA{\cdot}cm^{-2}$ and 0.3 $mAh{\cdot}cm^{-2}$; b) 0.6 $mA{\cdot}cm^{-2}$ and 0.6 $mAh{\cdot}cm^{-2}$; and for $Li_{6.4}Ge_{0.4}Sb_{0.6}S_5I$, a lower current density and capacity of c) 0.1 $mA{\cdot}cm^{-2}$ and 0.1 $mAh{\cdot}cm^{-2}$; and d) 0.3 $mA{\cdot}cm^{-2}$ and 0.3 $mAh{\cdot}cm^{-2}$ using a VMP3 potentiostat/galvanostat (Bio-Logic).

All-solid-state batteries employing the $Li_{6.7}Si_{0.7}Sb_{0.3}S_5I$ SSE in combination with a TiS_2 (or $LiCoO_2$) cathode and a Li-In alloy anode were assembled in an argon glovebox. First, ~ 80 mg of SSE powder was placed into a PEEK cylinder and cold pressed at 3 tons for 1 min (10 mm diameter). The composite cathode mixtures were prepared by mixing TiS_2 or $LiCoO_2$ and the SSE in an agate mortar at a weight ratio of 50:50 for TiS_2, and 70:30 for $LiCoO_2$. On one side of the SSE pellet, ~ 8 - 10 mg composite cathode mixture (37.4 mg for the high loading TiS_2 cell) was spread and pressed at 3 tons for 3 min. On the other side of the pellet, a thin indium foil (10 mm diameter, Alfa Aesar, 99.99%, 0.125 mm thickness) was attached and ~ 1 mg Li powder (FMC Lithium, ~ 2 mg for the high loading cell) was spread over the In foil, and pressed at 1.5 tons for 1 min. The cell was placed into a stainless steel casing with a constant applied pressure of ~ 1.5 tons. Galvanostatic cycling of the cell was carried out in the voltage range of 2.3 V - 3.7 V *vs* In/LiIn for the $LiCoO_2$ cell and 0.9 V - 2.4 V *vs* In/LiIn for the TiS_2 cell using a VMP3 (Bio-Logic) cycler.

Results

Structural evolution in the series $Li_{6+x}M_xSb_{1-x}S_5I$ (M = Si, Sn, Ge)

X-ray diffraction shows that the targeted synthesis of $Li_{6+x}Si_xSb_{1-x}S_5I$ ($0.1 \leq x \leq 0.7$) phases provide almost phase-pure polycrystalline powders in this solid solution range (**Fig. 1a**). All the phases were indexed in the same cubic space group, *F*-43*m,* that is adopted by most other argyrodites[3]. Higher Si^{4+} content ($x > 0.7$) leads to increasing amounts of impurities, indicative of the solubility limit (**Fig. S1a**). All solid solution phases exhibit very minor fractions of LiI and Li_2S (**Fig. 1a**). While the tiny Li_2S peak exhibits almost no change, the intensity of the LiI peaks increases with increasing Si^{4+} content, which correlates with I^- deficiency in the high-Si compositions as revealed by single crystal diffraction (see below). The argyrodite peaks shift to smaller *d*-spacing with increasing Si^{4+} content (**Fig. 1a**), because of substitution of Sb^{5+} with the

smaller Si^{4+} ion. Similar results are observed for Ge^{4+} and Sn^{4+} substituted $Li_{6+x}(Ge/Sn)_xSb_{1-x}S_5I$. **Fig. 1b** shows that phase pure $Li_{6+x}Ge_xSb_{1-x}S_5I$ ($0.1 \leq x \leq 0.4$) can be prepared, while for Sn substituted compositions, even at low content (x = 0.2), small impurities signal the limit of solubility, as shown in **Fig. 1b** and **S1b**.

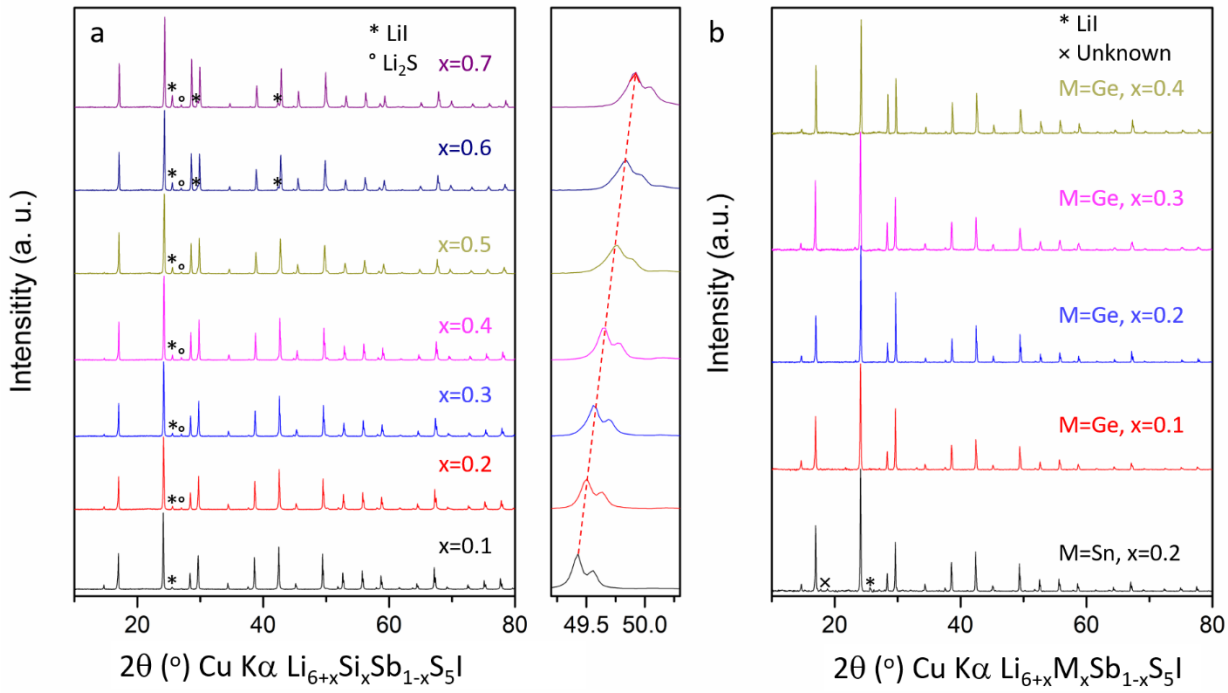

Figure 1. X-ray diffraction patterns of *as-synthesized* (a) $Li_{6+x}Si_xSb_{1-x}S_5I$ ($0.1 \leq x \leq 0.7$) and (b) $Li_{6+x}M_xSb_{1-x}S_5I$ (M = Sn, x= 0.2; M = Ge; $0.1 \leq x \leq 0.4$). All reflections correspond to the respective argyrodite phase except for the trace impurities as marked.

Ionic conductivity and Li^+ transport

Temperature-dependent impedance spectroscopy measurements were performed to determine the ionic conductivity of cold-pressed *as-synthesized* $Li_{6+x}M_xSb_{1-x}S_5I$ (M=Si, Sn, Ge) and the activation energy for Li-ion transport (**Fig. 2**). Arrhenius plots for all samples of $Li_{6+x}M_xSb_{1-x}S_5I$ (M=Si, Sn, Ge) are shown in **Fig. 2a - d,** and **Fig. S2,** and the activation energies are summarized in **Table S1**. Due to the high ionic conductivity of many of these phases, bulk and grain boundary contributions cannot be deconvoluted at room temperature. **Fig. 2e, f** shows the ionic conductivities of cold-pressed *as-synthesized* $Li_{6+x}Si_xSb_{1-x}S_5I$ and the extracted activation energy barriers for Li^+ diffusion, as measured by impedance spectroscopy **(Fig. S5)**. With increasing Si^{4+}+Li^+ content, the ionic conductivity increases dramatically, accompanied by a decrease in the activation energy from 0.41 eV (at x = 0) to about 0.25 eV (**Fig. 2e**). The highest

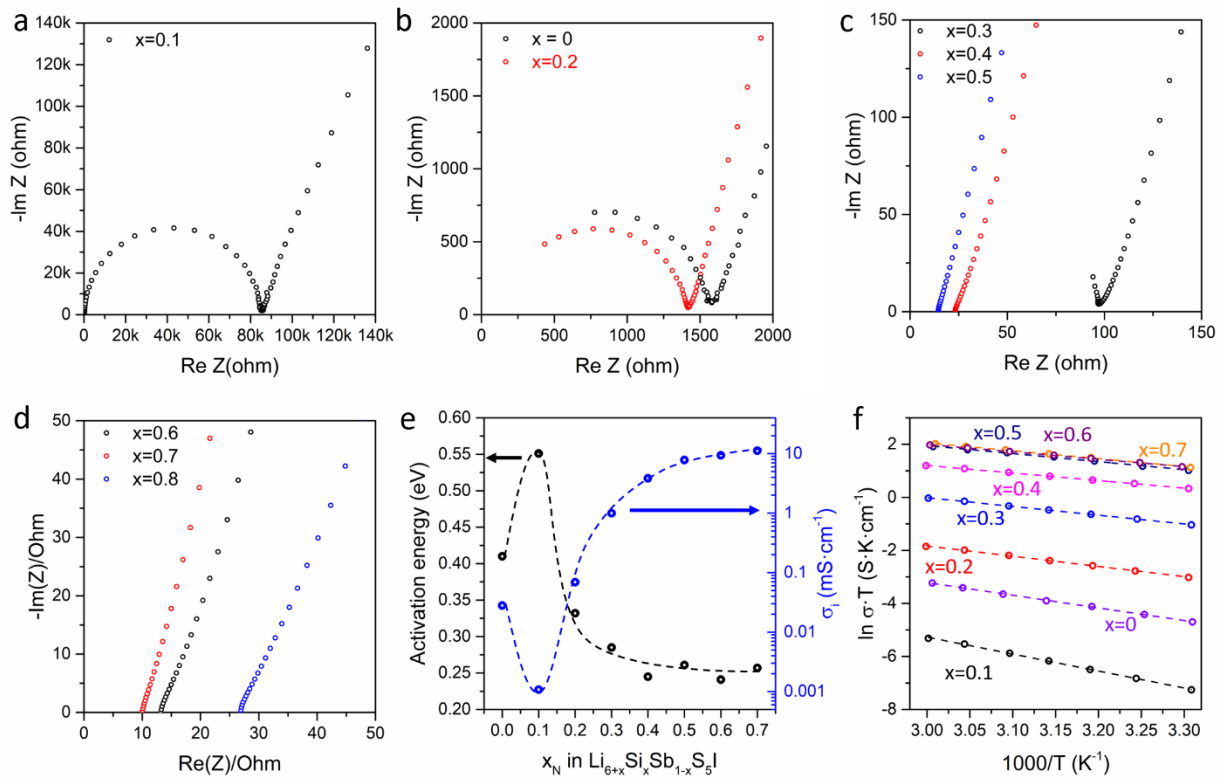

Figure 2. Nyquist plots (a) x = 0.1, (b) x= 0, 0.2, (c) x = 0.3, 0.4, 0.5 and (d) x = 0.6, 0.7, 0.8 for all degrees of substitution in the solid solution series $Li_{6+x}Si_xSb_{1-x}S_5I$ at room temperature; (e) activation energy and ionic conductivities of cold pressed *as-synthesized* $Li_{6+x}Si_xSb_{1-x}S_5I$ as a function of nominal Si^{4+} content (curves show the trend, and are not a fit of the data); (f) Arrhenius plots of the conductivity values for $Li_{6+x}Si_xSb_{1-x}S_5I$ in the temperature range from 30°C to 60°C. The anomalous low conductivity/high E_a value for x = 0.1 may be the result of an amorphous insulating material in the grain boundary (see text).

ionic conductivities were obtained in the range x = 0.6 - 0.7 of 9.4 and 11.2 mS·cm^{-1}, respectively; annealing these two materials **(Fig. S4)** further improved the cold-pressed pellet conductivity to 14.8 (x = 0.6) and 12.6 mS·cm^{-1} (x = 0.7). The ionic conductivity data for the cold-pressed pellets of *as-synthesized* and *annealed* materials is summarized in **Tables S1** and **S2**. The sintered pellets of x = 0.6, 0.7 exhibit an even higher ion conductivity, up to 24 mS·cm^{-1} for $Li_{6.6}Si_{0.6}Sb_{0.4}S_5I$, due to improved grain boundary contact (**Fig. S6** and **Table S3**) as discussed below. For the Sn^{4+} and Ge^{4+} substituted samples $Li_{6+x}(Ge/Sn)_xSb_{1-x}S_5I$, a similar trend (**Fig. S3**)is observed with increasing x but the corresponding conductivities are lower; the highest value reaches 6.25 mS·cm^{-1} for $Li_{6.4}Ge_{0.4}Sb_{0.6}S_5I$, and 0.12 mS·cm^{-1} for $Li_{6.2}Sn_{0.2}Sb_{0.8}S_5I$ (**Fig. S2** and **Table S1**).

To determine the grain boundary resistance, low temperature (195 K) measurements were conducted for selected Si-substituted compositions. **Fig. 3** shows Nyquist plots for $Li_{6+x}Si_xSb_{1-x}S_5I$ (x = 0.4 - 0.7). They exhibit two slightly depressed semicircles at high and mid frequencies and a

clear polarization spike at low frequencies. The spectra were fit with an equivalent circuit consisting of a serial connection of two parallel arrangements of a resistor (R) and a constant phase element (CPE, Q), representing the conductive and capacitive behaviors of the SSE, respectively, and an additional CPE component for polarization. For $Li_{6.7}Si_{0.7}Sb_{0.3}S_5I$, the capacitance of the high frequency semicircle is about two orders of magnitude lower than that for mid-frequency semicircle (details of the fits are listed in **Table S4**). Thus, the high-frequency semicircle is attributed to bulk (i.e., grain) conductivity and the mid-frequency semicircle is attributed to the grain boundary **(Fig. 3)**. At this low temperature of 195 K, significant grain boundary (GB) resistance was observed for all materials, as summarized in **Table 2**. This likely arises from the presence of a small fraction of ionically insulating material in the GB such as SiS_2. Because the GB conductivity is about eight fold lower than the bulk in all cases, it significantly lowers the total ionic conductivity. This explains why sintered pellets exhibit much higher σ_i (see above), which enhances GB contact.[30,32,33,47,48] It also may explain the anomalously low conductivity at the lowest value of x = 0.1, where a) a resistive GB component would have the most impact on total conductivity; b) homogeneous incorporation of a tiny amount of Si into the bulk may be difficult to achieve. Nonetheless, even at 195 K, all these materials still exhibit high bulk $\sigma_i > 0.1$ mS·cm^{-1} which is significantly higher than of an organic electrolyte at that temperature (**Fig. 3**). For the Ge^{4+} substituted sample $Li_{6.4}Ge_{0.4}Sb_{0.6}S_5I$, relatively high grain boundary resistance was also observed as shown in **Fig. S7** and **Table S5**.

Table 2. Bulk and grain boundary conductivities of *as-synthesized* $Li_{6+x}Si_xSb_{1-x}S_5I$ (x = 0.4 - 0.7, cold-pressed pellets) at 195 K.

Compositions	Bulk conductivity (mS·cm^{-1})	Grain boundary conductivity (mS·cm^{-1})
$Li_{6.7}Si_{0.7}Sb_{0.3}S_5I$	0.29	0.044
$Li_{6.6}Si_{0.6}Sb_{0.4}S_5I$	0.25	0.045
$Li_{6.5}Si_{0.5}Sb_{0.5}S_5I$	0.21	0.024
$Li_{6.4}Si_{0.4}Sb_{0.6}S_5I$	0.13	0.015

Owing to the high σ_i of the Si-substituted compositions, this family was targeted for single crystal, and powder X-ray synchrotron and neutron diffraction studies in order to correlate structure-property relationships as described below.

Structural characterization of $Li_{6+x}(Si/Ge/Sn)_xSb_{1-x}S_5I$ and Li^+ diffusion pathways

Li^+ argyrodite $Li_{6+x}Si_xSb_{1-x}S_5I$ ($0.1 \leq x \leq 0.7$) superionic conductors were synthesized with varying Si^{4+}/Sb^{5+} ratios in order to study the structural changes and assess the effect of increasing

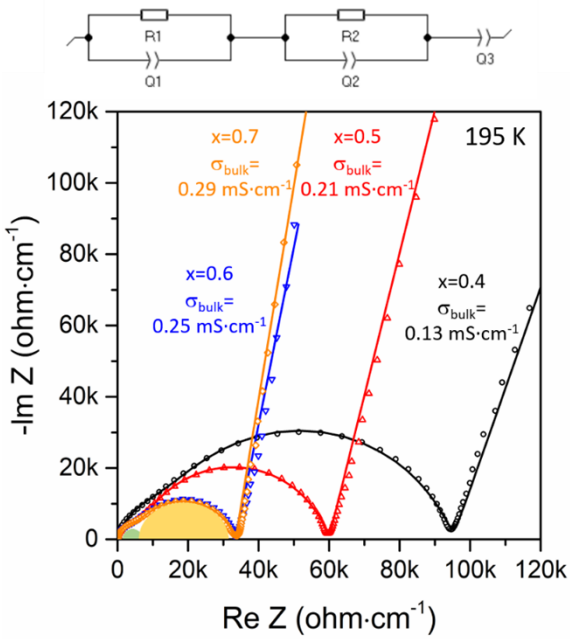

Figure 3. Low temperature (195 K) Nyquist plots for $Li_{6+x}Si_xSb_{1-x}S_5I$ (x = 0.4, 0.5, 0.6, 0.7) show two semicircles, corresponding to bulk and grain boundary contributions. The data was fit (shown by the line) with the equivalent circuit indicated.

Li^+ content on the σ_i. Single crystal diffraction was performed for crystals obtained at selected compositions (x = 0.1, 0.4, 0.5, 0.7) to determine the changes in Li site and S^{2-}/I^- disorder. As small compositional variance from crystal to crystal is always possible, powder X-ray synchrotron diffraction measurements were then conducted for all compositions to evaluate the overall sample purity, the solubility limit of Si^{4+}, and the degree of S^{2-}/I^- disorder. Due to the superionic conductivity of the Si-substituted compositions (i.e, very high Li^+ mobility), and hence possible location of some Li on alternative sites in the lattice that cannot be easily refined owing to very low occupation, single crystal diffraction results show slightly lower Li^+ content than experimental targeted values (see **Table S1**). Neutron powder diffraction measurements (300 K) were carried out to determine the Li^+ position and occupancy changes with different Si^{4+} content on selected compositions (x = 0, 0.3, 0.5, 0.7). In addition, low temperature (195 K) neutron powder diffraction was also conducted on $Li_{6.7}Si_{0.7}Sb_{0.3}S_5I$ to freeze out the Li^+ mobility, thus allowing more accurate determination of the Li^+ position and occupation.

The structure of the composition with the highest conductivity, $Li_{6.7}Si_{0.7}Sb_{0.3}S_5I$ (refined composition $Li_{6.77}Si_{0.66}Sb_{0.34}S_{5.01}I_{0.99}$) from the neutron diffraction study (**Fig. S9d**) is shown in **Fig. 4a, b, c** and compared to that of the classic phosphorus argyrodite Li_6PS_5I (**Fig. 4d, e**)[42]. The unit cell of the antimony phases adopts the same cubic space group *F*-43*m* as Li_6PS_5I (*a* =

10.1414(1) Å), but with a larger lattice parameter of a = 10.3231(1) Å, and a different Li^+ sublattice (four Li^+ sites) than typical Li^+-Argyrodite materials. A similar highly disordered cation distribution has also been identified in Ag^+/Cu^+-rich argyrodite.[49,50] Li ions still diffuse via three discrete jumps (doublet, intra and inter cage jumps) as for classic argyrodite Li_6PS_5X (X= Cl, Br, I), as shown in **Fig. 4e**.[42,51] The difference is that a new Li3(48*h*) site is identified in

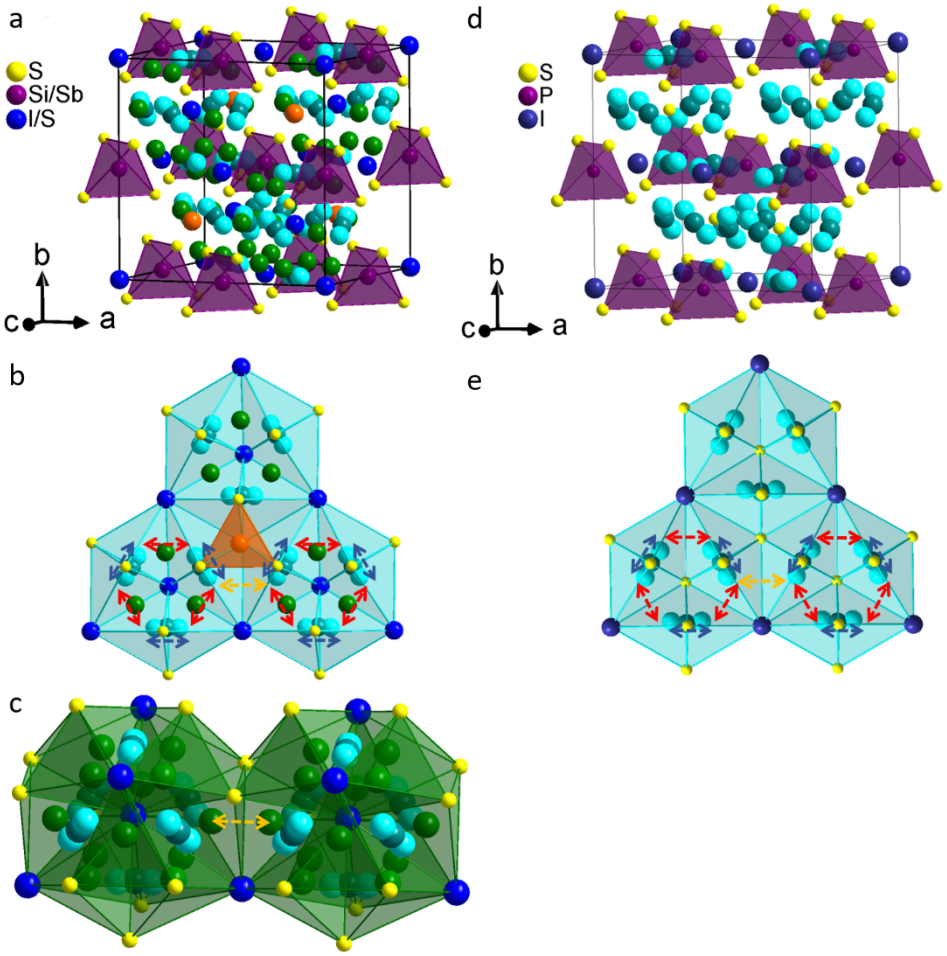

Figure 4. (a) Crystal structure of $Li_{6.7}Si_{0.7}Sb_{0.3}S_5I$ from powder neutron diffraction at 300 K, showing the fully occupied S (16*e*) site and the 2.6 and 1.7% S^{2-}/I^- (4*a,* 4*c*) mixed occupied site. $(Sb/Si)S_4$ tetrahedra are shown in dark violet. Four Li^+ sites exist: Li1(48*h*) - turquoise, Li2(24*g*) - teal, Li3(48*h*) - green, Li4(4*d*) - orange; (b) Li ion diffusion showing the discrete jumps: the doublet jump (Li1(48*h*)-Li1(48*h*) within bipyramids passing through Li2(24*g*), blue arrow), intracage jump (Li1(48*h*)-Li1(48*h*) within cage passing through the Li3(48*h*) site, red arrow) and intercage jump (Li1(48*h*)-Li1(48*h*) between cages, orange arrow); (c) new intercage jump Li3(48*h*)-Li3(48*h*) between cages is shown by the orange arrow; (d) crystal structure of Li_6PS_5I from ref. 42 is shown for comparison, with a fully ordered S (16*e*, 4*c*) and I (4*a*) arrangement. PS_4 tetrahedra are depicted in violet. The Li ion forms pseudo-octahedral cages (four/unit cell) with two crystallographically distinct sites, Li1(48*h*) and Li2(24*g*); (d) Li ion diffusion by discrete jumps: doublet jump (Li1(48*h*)-Li1(48*h*) within bipyramids passing through the Li2(24*g*) site, blue arrow); intracage jump (Li1(48*h*)-Li1(48*h*) within the cage, red arrow) and intercage jump (Li1(48*h*)-Li1(48*h*), orange arrow).

$Li_{6.7}Si_{0.7}Sb_{0.3}S_5I$ which resides between the intracage jump sites (**Fig. 4b**). This Li3(48*h*) site also creates a new intercage jump pathway (directly through the face-shared Li3(48*h*) tetrahedra, as shown in **Fig. 4c**. The crystallographic details of $Li_{6.7}Si_{0.7}Sb_{0.3}S_5I$ and $Li_{6+x}Si_xSb_{1-x}S_5I$ (x=0, 0.3, 0.5) phases are summarized in **Table 3** and **S6-9**. The structure exhibits one crystallographically distinct Sb/Si site for all compositions (x), which is partially occupied by Si (up to 70% in $Li_{6.7}Si_{0.7}Sb_{0.3}S_5I$) and is tetrahedrally coordinated by four S atoms. The refined lattice parameter (**Fig 5a**), $(Si_xSb_{1-x})S_4$ tetrahedral volume and (Si_xSb_{1-x})-S bond distance (**Fig. 5b**) from single crystal XRD (**Table S18 - 29**) and synchrotron XRD (**Table S10 - 17**) all decrease nearly linearly with increasing (Si^{4+} + Li^+) content in $Li_{6+x}Si_xSb_{1-x}S_5I$, indicating the formation of a solid solution in accordance with Vegard's law.

Table 3. Atomic coordinates, occupation factor and isotropic displacement parameter of representative $Li_{6.7}Si_{0.7}Sb_{0.3}S_5I$ obtained from powder neutron diffraction at 300 K.

a = 10.32309(5) Å, 4.32 wt% Li_2S, 6.43 wt% LiI						
Atom	Wyckoff Site	x	y	z	Occ.	U_{iso} (Å^2)
Li1	48*h*	0.290(1)	0.5175(9)	0.790(1)	0.29(2)	0.034(3)
Li2	24*g*	0.021(1)	0.25	0.25	0.34(3)	0.032(5)
Li3	48*h*	0.732(3)	0.067(2)	0.567(2)	0.097(9)	0.08(1)
Li4	4*d*	0.75	0.25	0.25	0.04(1)	0.01(2)
Si1	4*b*	0.5	0.5	0.5	0.655	0.0123(3)
Sb1	4*b*	0.5	0.5	0.5	0.345	0.0123(3)
S1	4*c*	0.25	0.25	0.25	0.983	0.0157(5)
S2	16*e*	0.3771(2)	0.3771(2)	0.6229(2)	1	0.0234(3)
S3	4*a*	0.5	0.5	0	0.026	0.0385(5)
I1	4*a*	0.5	0.5	0	0.974	0.0385(5)
I2	4c	0.25	0.25	0.25	0.017	0.0157(4)

The effect of S^{2-}/I^- site disorder in these materials merits discussion, in light of its proposed role in dictating conductivity in the argyrodites. From single crystal X-ray diffraction results, there is only slight (~1-2) % S^{2-}/I^- site disorder on the 4*a* and 4*c* site for x = 0.1 (**Fig. 5c**). At higher Li^+/Si^{4+} content (x > 0.1), only site disorder on the 4*a* site can be identified (but not on the 4*c* site) that increases with x to reach 7(1) % for the highly conductive phase (x = 0.7). We note that single crystal diffraction offers superior accuracy in determining the low degree of S^{2-}/I^- site disorder over any powder diffraction techniques. Most importantly, several percent of S^{2-}/I^- site disorder clearly will not lead to a three order of magnitude increase in σ_i compared to the parent phase (x = 0). This is further proved in the Ge and Sn substituted materials. Crystallographic details of

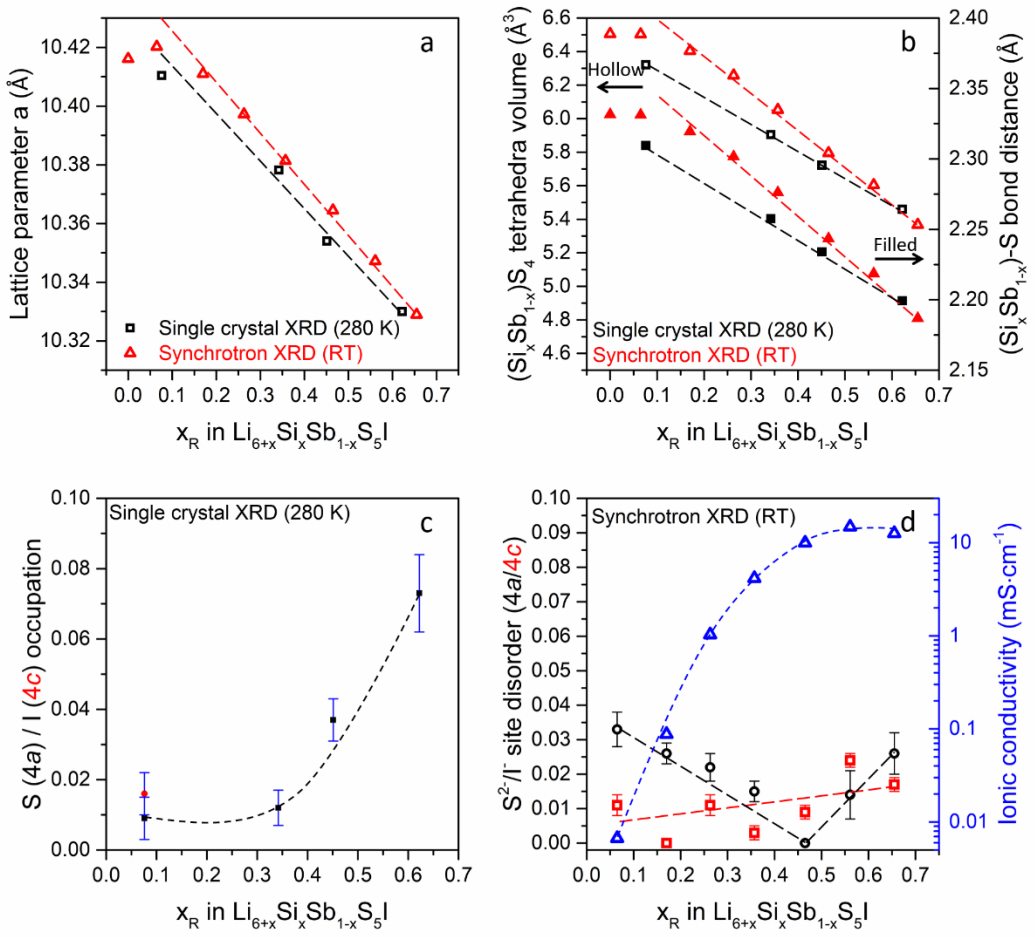

Figure 5. (a) lattice parameters, (b) $(Si_xSb_{1-x})S_4$ tetrahedral volume (left, hollow) and (Si_xSb_{1-x})-S bond distance (right, filled) of solid solutions $Li_{6+x}Si_xSb_{1-x}S_5I$ *vs* refined Si content (x_R) from single crystal XRD at 280 K (black) and synchrotron XRD at room temperature (red) and (c) S^{2-}/I^- disorder *vs* refined Si content (x_R) from single crystal XRD at 280 K; (d) S^{2-}/I^- site disorder and ionic as a function of refined Si content (x_R) from synchrotron diffraction measurements. Curves show the trend and are not a fit of the data.

$Li_{6+x}Ge_xSb_{1-x}S_5I$ (x= 0.2, 0.4) and $Li_{6.2}Sn_{0.2}Sb_{0.8}S_5I$ are summarized in **Table S30 - 38**) and the S^{2-}/I^- site disorder as a function of x and σ_i is shown in **Table 4**. For the Ge phase, even though x = 0.2 and 0.4 exhibit essentially the same anion disorder (~ 2.5%) σ_i increases by almost an order of magnitude from 0.87 $mS{\cdot}cm^{-1}$ for x = 0.2, to 6.3 $mS{\cdot}cm^{-1}$ for x = 0.4. The Sn phase at x = 0.2 shows slightly higher disorder but even lower ionic conductivity of 0.12 $mS{\cdot}cm^{-1}$. Furthermore, as small compositional variance from crystal to crystal is always possible, powder synchrotron diffraction measurements (**Fig. S10**) were conducted for annealed $Li_{6+x}Si_xSb_{1-x}S_5I$ ($0.1 \leq x \leq 0.7$) compositions. **Fig. 5d** confirms that upon annealing, there is no obvious correlation between S^{2-}/I^- site disorder and conductivity. Overall, the annealed samples show slightly higher ionic

conductivity compared to non-annealed samples but yet all materials exhibit < 3.3 % S^{2-}/I^- site disorder. Thus, the compositions $Li_{6+x}M_xSb_{1-x}S_5I$ (M = Si, Sn, Ge) exhibit very high ionic conductivity with a low degree of S^{2-}/I^- disorder, and the latter is ruled out as a major contributing factor.

Table 4. S^{2-}/I^- site disorder from single crystal X-ray diffraction at 280 K and ionic conductivities at room temperature for $Li_{6+x}M_xSb_{1-x}S_5I$ (M=Sn, Ge).

$Li_{6+x}M_xSb_{1-x}S_5I$			
S^{2-}/I^- disorder	M=Sn, x=0.2	M=Ge, x=0.2	M=Ge, x=0.4
4*a* site	1.0(2) %	2.4(6) %	2.6(5) %
4*c* site	4.4(6) %	1.2(7) %	2.2(5) %
Ionic conductivity ($mS.cm^{-1}$)	0.12	0.87	6.3

Interfacial stability with Li metal

The Li plating/stripping behavior and interfacial stability of $Li_{6.7}Si_{0.7}Sb_{0.3}S_5I$ towards a Li metal anode were evaluated in symmetric Li | $Li_{6.7}Si_{0.7}Sb_{0.3}S_5I$ | Li cells. $Li_{6.7}Si_{0.7}Sb_{0.3}S_5I$ exhibited excellent stability with Li metal, exhibiting a steady voltage profile at a current of 0.3 $mA{\cdot}cm^{-2}$ and capacity of 0.3 $mAh{\cdot}cm^{-2}$ for 600 hours. At even a higher current of 0.6 $mA{\cdot}cm^{-2}$ and capacity of 0.6 $mAh{\cdot}cm^{-2}$, stripping/plating continued up to a total of 1000 hours (**Fig 6a**). **Fig. 6b** shows that the initial cell voltage for the cell cycled at 0.3 $mA{\cdot}cm^{-2}$ increases slightly from 7.3 mV to 11.3 mV after 600 hours, and then a stable voltage profile at 22.0 mV was observed for another 400 hours at current density of 0.6 $mA{\cdot}cm^{-2}$. Nyquist plots of cell impedance are shown in **Fig. 6c**, directly after contact of the Li metal and SSE; after 600 hours cycling at 0.3 $mA{\cdot}cm^{-2}$; and after an additional 400 hours cycling at 0.6 $mA{\cdot}cm^{-2}$. While the spectra cannot be fit well with an equivalent circuit, it is nonetheless very clear that the total resistivity increases slightly during cycling and then stabilizes at a relatively low value (**Fig. 6c**). Furthermore, $Li_{6.4}Ge_{0.4}Sb_{0.6}S_5I$ also exhibits relatively stable Li stripping/plating (albeit at lower current density and capacity) up to 0.3 $mA{\cdot}cm^{-2}$ and 0.3 $mAh{\cdot}cm^{-2}$ (**Fig. S11a**), which is still much more stable compared to other Ge-containing materials such as LGPS or even protected LGPS.[22,52,53] At higher current density of 0.6 $mA{\cdot}cm^{-2}$ (**Fig. S11b**), microshorts appear (in contrast to $Li_{6.7}Si_{0.7}Sb_{0.3}S_5I$ at that same current, which is exhibits a steady profile). Nyquist plots of cell impedance are shown in **Fig. S11c**, which shows the total resistivity increases during cycling and then stabilizes. We note that recent work indicates the pressure-dependent critical stripping current can lead to Li voids and dendrite

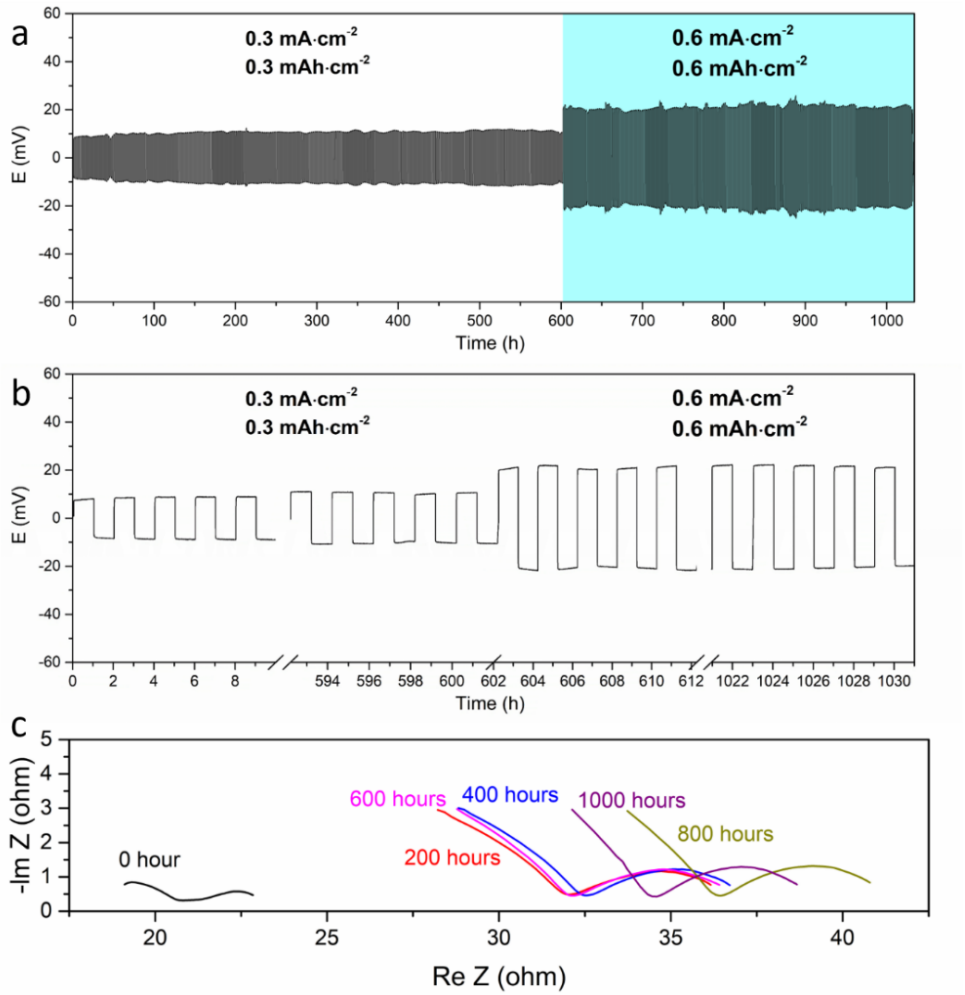

Figure 6. (a) the voltage profile of Li^+ plating/stripping in a Li | $Li_{6.7}Si_{0.7}Sb_{0.3}S_5I$ | Li symmetric cell, cycled at different currents and capacities (0.3 mA·cm^{-2} and 0.3 mAh·cm^{-2} for 600 h; 0.6 mA·cm^{-2}, 0.6 mAh·cm^{-2} (blue) for another 400 h); (b) enlarged voltage profiles of the Li | $Li_{6.7}Si_{0.7}Sb_{0.3}S_5I$ | Li symmetric cell of the first and last 10 cycles at different current densities; (c) Nyquist plots of the Li | $Li_{6.7}Si_{0.7}Sb_{0.3}S_5I$ | Li symmetric cell: before cycling (0 h, black); cycling at 0.3 mA·cm^{-2} and 0.3 mAh·cm^{-2} for 200 h (red), 400 h (blue) and 600 h (magenta); cycling at 0.6 mA·cm^{-2}, 0.6 mAh·cm^{-2} for another 200 h (800 h in total, dark yellow) and 400 h (1000 h in total, purple).

formation,[54] whereas microstructural characteristics of a garnet SSE lead to locally differing Li deposition kinetics and morphologies.[55] Further densification, surface polishing of the argyrodite pellet and control of applied pressure will possibly enable stable Li plating/stripping at even higher current density and capacity. Nevertheless, the stable symmetric cell cycling, steady voltage profile and stable total resistivity all indicate formation of a relatively stable interphase between Li metal and $Li_{6.7}Si_{0.7}Sb_{0.3}S_5I$ which is favorable to ultimately develop a long-life Li-metal ASSB.

All solid state battery

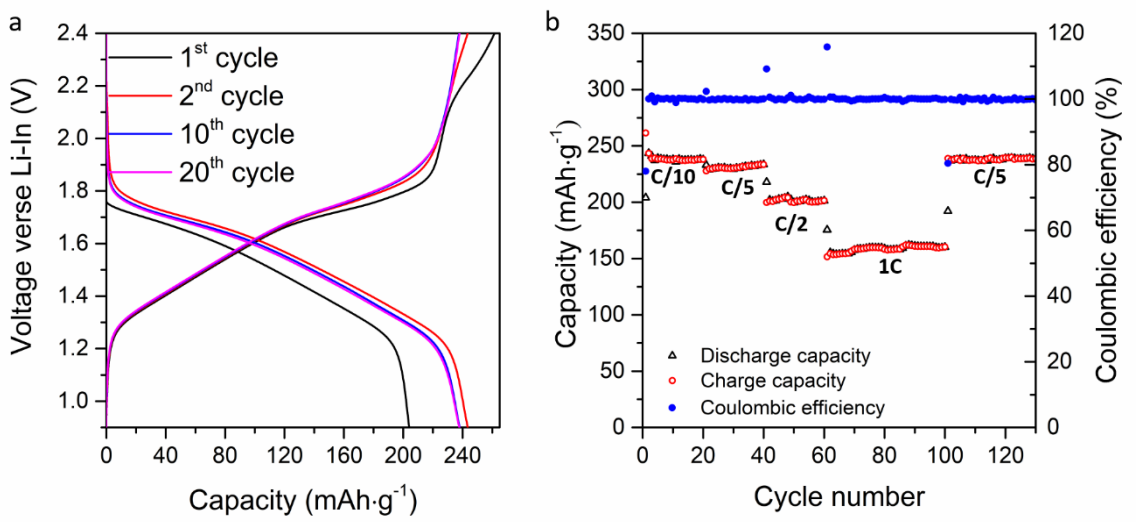

Figure 7. Electrochemical performance of TiS_2/Li-In ASSBs using $Li_{6.7}Si_{0.7}Sb_{0.3}S_5I$ as the solid electrolyte at room temperature. (a) 1st, 2nd, 10th, 20th cycle discharge-charge voltage profiles at C/10. (b) discharge-charge capacity and the Coulombic efficiency (CE) as a function of cycle number at different C-rates.

To further evaluate the electrochemical properties of these new superionic conductors, prototype cells were assembled with $Li_{6.7}Si_{0.7}Sb_{0.3}S_5I$, where a Li-In alloy as the negative electrode was paired with TiS_2 or $LiCoO_2$ as the positive. These choices were made in order to more clearly showcase the conductive properties of the solid electrolyte. Pairing the SSE with Li metal and high voltage positive electrodes will be the topic of future work devoted to ASSBs. **Fig. 7a** shows the 1st, 2nd, 10th, and 20th cycle discharge-charge voltage profiles for the TiS_2 cell cycled at 0.1 C between 0.9 and 2.4 V at room temperature. A highly reversible capacity of 240 $mAh{\cdot}g^{-1}$ is exhibited, corresponding to the theoretical value for TiS_2. The discharge/charge capacity at different C-rates and the Coulombic efficiencies are displayed in **Fig. 7b** (see **Fig. S12** for the corresponding voltage profiles). At a practical rate of C/5, the cell still retains almost 100% theoretical capacity after 130 cycles, and delivers ~ 85% capacity (200 $mAh{\cdot}g^{-1}$) at a C/2 rate. The cell delivers somewhat lower capacity at 1C (~70% of theoretical capacity), possibly due to the slight oxidation of SSE on the 1st charge shown in **Fig. 7a** (SSE oxidation occurs at ~2.1 V vs Li-In). Slow Li-ion diffusion kinetics in the Li-In alloy may also be responsible. Furthermore, a high loading cell (23.8 $mg{\cdot}cm^{-2}$ TiS_2) also exhibits highly reversible, theoretical capacity (close to 240 $mAh{\cdot}g^{-1}$) at C/10, as shown in **Fig. S13**. The $LiCoO_2$ cell (**Fig. S14**) also exhibits relatively stable cycling, though the capacity fades due to an insulating interface build-up between the $LiCoO_2$ and $Li_{6.7}Si_{0.7}Sb_{0.3}S_5I$. This naturally results from oxidation of the SSE at the higher voltage of the

$LiCoO_2$ positive electrode, since a protective coating layer was not used on the oxide in these preliminary studies. Overall, the respectable electrochemical performance for the ASSBs using $Li_{6.7}Si_{0.7}Sb_{0.3}S_5I$ highlights its very high room temperature Li^+ conductivity.

Discussion: origin of the superionic conductivity of $Li_{6+x}M_xSb_{1-x}S_5I$ - concerted ion migration mechanism

A summary of the results above indicates that the aliovalent substitution of ($Li^+ + M^{4+}$) for Sb^{5+} in $Li_{6+x}M_xSb_{1-x}S_5I$ (M=Si, Sn, Ge) - and hence increased Li^+ concentration and altered distribution - tremendously influences the Li^+ ion conductivity in the argyrodite structure even at low levels of x. A superionic conductivity of 14.8 $mS{\cdot}cm^{-1}$ (cold-pressed pellet) for the optimal composition $Li_{6.6}Si_{0.6}Sb_{0.4}S_5I$ is accompanied by a low activation energy barrier for Li^+ diffusion of 0.25 eV. Structure solution from powder X-ray synchrotron/neutron and single crystal diffraction shows a slight increase in the S^{2-}/I^- site disorder over the 4*a*/*c* site in the Si phases $Li_{6+x}Si_xSb_{1-x}S_5I$ with increasing x, but this is small even for the x= 0.7 composition (up to 7% for single crystal measurements, and up to 3.3 % for synchrotron diffraction measurements on *annealed* samples). As recently experimentally and theoretically suggested,[33,38,42] disorder between sulfide and halide can lead to lower activation barriers. However, such low level S^{2-}/I^- site disorder does not lead to the three-order of magnitude increase in σ_I we observe here. It has also been suggested that high multiplicity of the Li^+ site can make percolation possible at a low degree of disorder.[33] We note that $Li_{6.6}Si_{0.6}Sb_{0.4}S_5I$ shows tripled ionic conductivity compared to $Li_{6.6}Ge_{0.6}P_{0.4}S_5I$: namely 14.8 $mS{\cdot}cm^{-1}$ *vs* 5.4 $mS{\cdot}cm^{-1}$, respectively (measurements being both conducted on cold-pressed materials). The increased ionic conductivity can be ascribed to the different Li^+ distribution between these materials (as discussed below).

In the stoichiometric Li_6PnS_5I (Pn = P, Sb) argyrodite structure, Li^+ occupies tetrahedral sites: each site shares a common face with one other to form a bipyramid; in turn, each bipyramid shares an edge with another bipyramid and six bipyramids form a cage (**Fig. 4**, above). In one unit-cell, there are 4 cages (24 bipyramids) and each bipyramid is occupied by one Li^+ that can only move freely within the bipyramid (equilibrium state). To sustain macroscopic Li ion diffusion, a defect formation step is necessary and the sum of defect formation and migration energies correspond to a high activation energy as measured by EIS. This is further supported by a DFT MD simulation of Li_6PS_5I[38] which shows inter and intra cage jumps pass through a much higher activation barrier than that in Li_6PS_5Cl and Li_6PS_5Br as depicted in **Fig. 8a**, which leads to low σ_i.

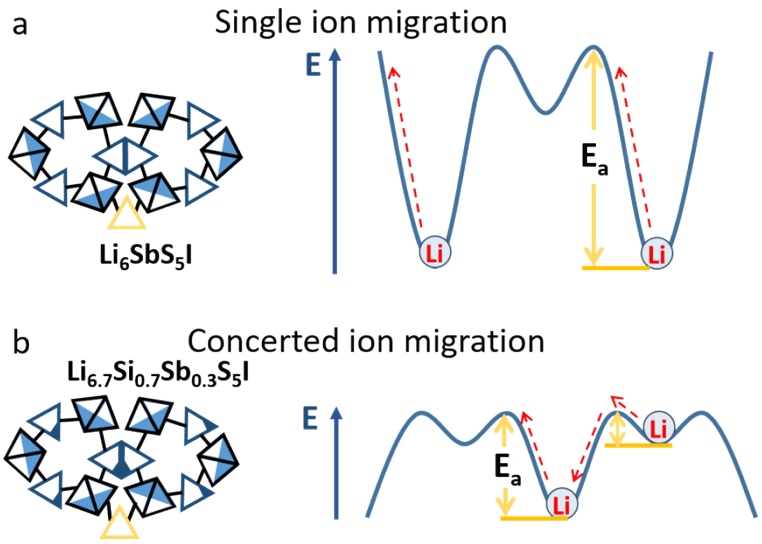

Figure 8. Proposed mechanism of (a) traditional vacancy Li ion diffusion mechanism for Li_6SbS_5I and (b) concerted Li ion migration with a flatter energy landscape induced by Li ion site disorder. The triangle indicates a tetrahedral site, and the filled ones indicate a partially occupied site. The empty sites are depicted by an open triangle. The energy landscape is shown for the intracage jump. Black triangles: Li1(48*h*); blue triangles: Li3(48*h*), unoccupied site for Li_6SbS_5I; yellow triangles: unoccupied sites on the pathway on the intercage jump pathway.

However, in Li-rich $Li_{6+x}Si_xSb_{1-x}S_5I$, our neutron diffraction analysis (**Fig. S8**) reveals a different Li^+ sublattice than other typical Li-argyrodites and the previously-reported Li-rich $Li_{6.6}Ge_{0.6}P_{0.4}S_5I$[33,43]. Two new Li^+ sites, along with the original two sites in Li_6SbS_5I, are identified. These sit within the Li^+ cages at the mid-point of the intra-cage jump and between the Li^+ cages at the mid-point of the inter-cage jump with relatively low occupancy (**Fig. 4b-c, Table 3**). They can be regarded as high-energy interstitial sites for Li^+ diffusion. The occupancy of the Li3(48*h*) site increases with increasing Li^++Si^{4+} content, and meanwhile creates vacancies on the Li1(48*h*)-Li2(24*g*)-Li1(48*h*) equilibrium sites (within one bipyramid), as shown in **Fig. S15a** (we do not speculate on the role of the Li4(4*d*) site due to its very low occupancy, **Table 3**). The redistribution of Li^+ from Li1-2 onto the Li3 sites and hence creation of vacancies on those sites help eliminate the defect formation step for Li^+ diffusion. The increased Li^+ concentration in $Li_{6+x}Si_xSb_{1-x}S_5I$ pushes the additional Li^+ ions into these high-energy interstitial sites. These positions are very close (~ 1.6 Å) to the low energy sites with higher occupancy and increase the Li^+-Li^+ interactions. Thus the site energies of Li1 and Li3 become closer with increasing Li^+ content, as both increase due to Coulombic repulsion (**Fig. S15b**). The resultant repulsion will activate concerted ion migration[56] with a significantly lower activation energy for Li-ion diffusion, as described schematically in **Fig. 8b**. The new intercage jump (**Fig. 4c**) - directly through the face-shared

Li3(48*h*) tetrahedra with a presumed low activation energy barrier[57] - connects the Li^+ cages in the unit cell and should also favor macroscopic long-range Li ion diffusion (superionic conductivity). These high-energy interstitial sites for diffusion indicate the existence of local minima with no strongly preferred positions which leads to an overall lowering of the activation energy.[58,59,60,61] A similar principle was identified in Li-stuffed garnets. The garnet-type compounds $Li_5La_3M_2O_{12}$ (M = Nb, Ta) initially were reported to exhibit a Li-ion conductivity of $\sim 10^{-6}$ at 25 °C, but substitution on the La and M sites by lower-valent metal ions led to Li-rich garnet-type materials, where conductivities of 1 $mS \cdot cm^{-1}$ are achieved.[62]

Conclusions

Exploration of the series $Li_{6+x}M_xSb_{1-x}S_5I$ (M=Si, Sn, Ge) reveals a highly promising sulfide solid-state electrolyte, $Li_{6.6}Si_{0.6}Sb_{0.4}S_5I$ that exhibits superionic conductivity owing to a unique framework with minor S^{2-}/I^- anion disorder and a distinctly disordered Li^+ distribution. Using a combination of single crystal and powder synchrotron and neutron diffraction and impedance spectroscopy, changes in the Li^+ occupancies and S^{2-}/I^- anion disorder across the series were monitored for the Si members of the series. With increasing substitution of Si^{4+} onto the Sb^{5+} site and Li^+ into the lattice, a significant lowering of the activation energy barrier for Li ion mobility is related to the slightly increased S^{2-}/I^- site disorder but mostly to the disordered Li^+ distribution. The additional Li^+ ions populate high-energy interstitial sites, thus activating concerted ion migration. This process further leads to a very low activation energy barrier and superionic conductivity of 14.8 $mS \cdot cm^{-1}$ for cold pressed $Li_{6.6}Si_{0.6}Sb_{0.4}S_5I$ which can be utilized in ASSBs. The ionic conductivity can be further increased by decreasing the grain boundary contributions, and thus sintered pellets exhibit a higher σ_i of 24 $mS \cdot cm^{-1}$. Furthermore, the new superionic conductors exhibit good stability with Li metal, where no apparent microshorts were evident even at high current density stripping/plating experiments conducted at 0.6 $mA \cdot cm^{-2}$ at a capacity 0.6 $mAh \cdot cm^{-2}$. Excellent electrochemical performance is observed for a prototype TiS_2/LiIn all-solid state battery, which augers well for the future development of advanced all-solid-state Li metal batteries. Most importantly, our work shows that structural changes leading to Li^+ site disorder can induce alterations to the potential energy landscape for the mobile Li ions in fast-ion conductors; namely (as predicted theoretically),[63] pushing Li^+ ions into high energy sites will induce concerted ion migration with a reduced migration energy barrier in Li-rich phases. This strategy should prove

invaluable for further optimizing solid electrolyte materials towards high ionic conductivity, new material discovery and allow the commercialization and practical use of ASSBs.

Supporting Information

XRD patterns; Nyquist plots and equivalent circuit fitting results; ionic conductivity; complete single crystal structure data and synchrotron/neutron Rietveld refinement results; Symmetric cell data; ASSBs data.

Crystallographic data

AUTHOR INFORMATION

Corresponding Author

lfnazar@uwaterloo.ca

ORCID

Linda F. Nazar: 0000-0002-3314-8197

Laidong Zhou: 0000-0002-8556-3296

Notes

The authors declare no competing financial interests.

Acknowledgments

This research was supported by the BASF International Scientific Network for Electrochemistry and Batteries. L.F.N. also thanks NSERC for generous support via their Canada Research Chair and Discovery Grant programs. Neutron diffraction measurement at the POWGEN instrument at Oak Ridge National Laboratory, Spallation Neutron Source, was sponsored by the Scientific User Facilities Division, Office of Basic Energy Sciences, US Department of Energy. We would like to thank Dr. Melanie Kirkham for the neutron powder diffraction data collection. Synchrotron XRD measurements were performed using beamline 08B1-1 at the Canadian Light Source, which is supported by the Canada Foundation for Innovation, Natural Sciences and Engineering Research Council of Canada, the University of Saskatchewan, the Government of Saskatchewan, Western Economic Diversification Canada, the National Research Council Canada, and the Canadian Institutes of Health Research. We would also like to thank Dr. Joel Reid for the synchrotron X-ray powder diffraction data collection.

REFERENCES

(1) Janek, J.; Zeier, W. G. A Solid Future for Battery Development. *Nat. Energy* **2016**, *1*, 16141.

(2) Goodenough, J. B.; Park, K. The Li-ion Rechargeable Battery: A perspective. *J. Am. Chem. Soc.* **2013**, *135*, 1167-1176.

(3) Bachman, J. C.; Muy, S.; Grimaud, A.; Chang, H. H.; Pour, N.; Lux, S. F.; Paschos, O.; Maglia, F.; Lupart, S.; Lamp, P.; Ciordano, L.; Yang, S. H. Inorganic Solid-State Electrolytes for Lithium Batteries: Mechanism and Properties Governing Ion Conduction. *Chem. Rev.* **2015**, *116*, 140-162.

(4) Zhang, Z.; Shao, Y.; Lotsch, B.; Hu, Y. S.; Li, H.; Janek, J.; Nazar, L. F.; Nan, C. W.; Maier, J.; Armand, A.; Chen, L. New Horizons for Inorganic Solid State Ion Conductors. *Energy Environ. Sci.* **2018**, *11*, 1945-1976.

(5) Culver, S. P.; Koerver, R.; Krauskopf, T.; Zeier, W. G. Designing Ionic Conductors: The Interplay between Structural Phenomena and Interfaces in Thiophosphate-Based Solid-State Batteries. *Chem. Mater.* **2018**, *30*, 4179-4192.

(6) Liu, Z.; Fu, W.; Payzant, W. A.; Yu, X.; Wu, Z.; Dudney, N. J.; Kiggans, J.; Hong, K.; Rondinone, A. J.; Liang, L. Anomalous High Ionic Conductivity of Nanoporous β-Li_3PS_4. *J. Am. Chem. Soc.* **2013**, *135*, 975-978.

(7) Rangasamy, E.; Liu, Z.; Gobet, M.; Pilar, K.; Sahu, G.; Zhou, W.; Wu, H.; Greenbaum, S.; Liang, C. An Iodide-Based $Li_7P_2S_8I$ Superionic Conductor. *J. Am. Chem. Soc.* **2015**, *137*, 1384-1387.

(8) Bron, P.; Johansson, S.; Zick, K.; Schmedt auf der Günne, J.; Dehnen, S.; Roling, B. $Li_{10}SnP_2S_{12}$: An Affordable Lithium Superionic Conductor. *J. Am. Chem. Soc.* **2013**, *135*, 15694-15697.

(9) Park, S. S.; Tulchinsky, Y.; Dincă, M. Single-Ion Li^+, Na^+, and Mg^{2+} Solid Electrolyte Supported by a Mesoporous Anionic Cu-Azolate Cu-Azolate Metal-Organic Framework *J. Am. Chem. Soc.* **2017**, *139*, 13260-13263.

(10) Hu, Y.; Dunlap, N.; Wan, S.; Lu, S.; Huang, S.; Sellinger, I.; Ortiz, M.; Jin, Y.; Lee, S.; Zhang, W. Crystalline Lithium Imidazolate Covalent Organic Frameworks with High Li-Ion Conductivity. *J. Am. Chem. Soc.* **2019**, *141*, 7518-7525.

(11)Miner, E. M.; Park, S. S.; Dincă, M. High Li^+ and Mg^{2+} Conductivity in a Cu-Azolate Metal–Organic Framework. *J. Am. Chem. Soc.* **2019**, *141*, 4422-4427.

(13) Wang, Z.; Santhanagopalan, D.; Zhang, W.; Wang, F.; Xin, H. L.; He, K.; Li, J.; Dudney, N.; Meng, Y. S. In Site STEM-EELS Observation of Nanoscale Interfacial Phenomena in All-Solid-State Batteries. *Nano Lett.* **2016**, *16*, 3760-3767.

(14) Walther, F.; Koerver, R.; Fuchs, T.; Ohno, S.; Sann, J.; Rohnke, M.; Zeier, W. G.; Janek, J. Visualization of the Interfacial Decomposition of Composite Cathodes in Argyrodite-Based All-Solid-State Batteries Using Time-of-Flight Secondary-Ion Mass Spectrometry. *Chem. Mater.* **2019**, *31*, 3745-3755.

(15) Wang, S. F.; Xu, H.; Li, W.; Dolocan, A.; Manthiram, A. Interfacial Chemistry in Solid-State Batteries: Formation of Interphase and Its Consequences. *J. Am. Chem. Soc.* 2018, **140**, 250-257.

(16) Wenzel, S.; Sedlmaier, S. J.; Dietrich, C.; Zeier, W. G.; Janek, J. Interfacial Reactivity and Interphase Growth of Argyrodite Solid Electrolytes at Lithium Metal Electrodes. *Solid State Ionics* **2018**, *318*, 102-112.

(17) Hood, Z. D.; Wang, H.; Pandian, A. S.; Keum, J. K.; Liang, C. Li_2OHCl Crystalline Electrolyte for Stable Metallic Lithium Anodes. *J. Am. Chem. Soc.* **2016**, *138*, 1768-1771.

(18) Luo, W.; Gong, Y.; Zhu, Y.; Fu, K. K.; Dai, J.; Lacey, S. D.; Wang, C.; Liu, B.; Han, X.; Mo, Y.; Wachsman, E. D.; Hu, L. Transition from Superlithiophobicity to Superlithiophilicity of Garnet Solid-State Electrolyte. *J. Am. Chem. Soc.* **2016**, *138*, 12258-12262.

(19) Li, Y.; Chen, X.; Dolocan, A.; Cui, Z.; Xin, S.; Xue, L.; Xu, H.; Park, K.; Goodenough, J. B. Garnet Electrolyte with an Ultralow Interfacial Resistance for Li-Metal Batteries. *J. Am. Chem. Soc.* **2018**, *140*, 6448-6455.

(20) Santhanagopalan, D.; Qian, D.; McGilvray, T.; Wang, Z.; Wang, F.; Camino, F.; Graetz, J.; Dudney, N.; Meng Y. S. Interface Limited Lithium Transport in Solid-State Batteries. *J. Phys. Chem. Lett.* **2014**, *5*, 298-303.

(21) Zhang, W.; Weber, D. A.; Weigand,H.; Arlt, T.; Manke, I.; Schröder, D.; Koerver, R.; Leichtweiss, T.; Hartmann, P.; Zeier, W. G.; Janek, J. Interfacial Processes and Influence of Composite Cathode Microstructure Controlling the Performance of All-Solid-State Lithium Batteries. *ACS Appl. Mater. Interfaces* **2017**, *9*, 17835-17845.

(12) Manthiram, A.; Yu, X.; Wang, S. Lithium Battery Chemistries enabled by Solid-State Electrolytes. *Nat. Rev. Mater.* **2017**, *2*, 16103-16118.

(22) Zhang, Z.; Chen, S.; Yang, J.; Wang, J.; Yao, L.; Yao, X.; Cui, P.; Xu, X. Interface Re-Engineering of $Li_{10}GeP_2S_{12}$ Electrolyte and Lithium anode for All-Solid-State Lithium Batteries with Ultralong Cycle Life. *ACS Appl. Mater. Interfaces* **2018**, *10*, 2556-2565.

(23) Pang, Q.; Liang, X.; Shyamsunder, A.; Nazar, L. F. An *In Vivo* Formed Solid Electrolyte Surface Layer Enables Stable Plating of Li Metal. *Joule* **2017**, *1*, 871-886.

(24) Pang, Q.; Zhou, L.; Nazar, L. F. Elastic and Li-Ion–Percolating Hybrid Membrane Stabilizes Li Metal Plating. *Proc. Natl. Acad. Sci.* **2018**, *115*, 12389-12394.

(25) Liang, J.; Zeng, X.; Zhang, X.;T. Zuo, T.; Yan, M.; Yin, Y.; Shi, J.; Wu, X.; Guo, Y.; Wan, L. Engineering Janus Interfaces of Ceramic Electrolyte via Distinct Functional Polymers for Stable High-Voltage Li-Metal Batteries. *J. Am. Chem. Soc.* **2019**, *141*, 9165-9169.

(26) Duan, H.; Yin, Y.; Shi, Y.; Wang, P.; Zhang, X.; Yang, C.; Shi, J.; Wen, R.; Guo, Y.; Wan, L. Dendrite-Free Li-Metal Battery Enabled by a Thin Asymmetric Solid Electrolyte with Engineered Layers. *J. Am. Chem. Soc.* **2018**, *140*, 82-85.

(27) Koerver, R.; Zhang, W.; de Biasi, L.; Schweidler, S.; Kondrakov, A. O.; Kolling,S.; Brezesinski, T.; Hartmann, P.; Zeier, W. G.; Janek, J. Chemo-Mechanical Expansion of Lithium Electrode Materials – on the Route to Mechanically Optimized All-Solid-State Batteries. *Energy Environ. Sci.* **2018**, *11*, 2142−2158.

(28) Kato, Y.; Shiotani, S.; Morita, K.; Suzuki, K.; Hirayama, M.; Kanno, R. All-Solid-State Batteries with Thick Electrode Configurations. *J. Phys. Chem. Lett.* **2018**, *9*, 607-613.

(29) Kamaya, N.; Homma, K.; Yamakawa, Y.; Hirayama, M.; Kanno, R.; Yonemura, M.; Kamiyama, T.; Kato, Y.; Hama, S.; Kawamoto, K.; Mitsui, A. A Lithium Superionic Conductor. *Nat. Mater.* **2011**, *10*, 682-686.

(30) Sun, Y.; Suzuki, K.; Hori, S.; Hirayama, M.; Kanno, R. Superionic Conductors: $Li_{10+\delta}[Sn_ySi_{1-y}]_{1+\delta}P_{2-\delta}S_{12}$ with a $Li_{10}GeP_2S_{12}$-type Structure in the Li_3PS_4-Li_4SnS_4-Li_4SiS_4 Quasi-ternary System. *Chem. Mater.* **2017**, *29*, 5858-5864.

(31) Kato, Y.; Hori, S.; Saito, T.; Suzuki, K.; Hirayama, M.; Mitsui, A.; Yonemura, M.; Iba, H.; Kanno, R. High-Power All-Solid-State Batteries using Sulfide Superionic Conductors. *Nat. Energy* **2016**, *1*, 16030.

(32) Seino, Y.; Ota, T.; Takada, K.; Hayashi, A.; Tatsumisago, M. A Sulphide Lithium Super Ion Conductor is Superior to Liquid Ion Conductors for Use in Rechargeable Batteries. *Energy Environ. Sci.* **2014**, *7*, 627-631.

(33) Kraft, M. A.; Ohno, S.; Zinkevich, T.; Koerver, R.; Culver, S. P.; Fuchs, T.; Senyshyn, A.; Indris, S.; Morgan, B. J.; Zeier, W. G. Inducing High Ionic Conductivity in the Lithium Superionic Argyrodites $Li_{6+x}P_{1-x}Ge_xS_5I$ for All-Solid-State Batteries. *J. Am. Chem. Soc.* **2018**, *140*, 16330-16339.

(34) Deiseroth, H. J.; Kong, S. T.; Eckert, H.; Vannahme, J.; Reiner, C.; Zaiß, T.; Schlosser, M. Li_6PS_5X: A Class of Crystalline Li-Rich Solids With an Unusually High Li^+ Mobility. *Angew. Chem., Int. Ed.* **2008**, *47*, 755−758.

(35) Ryavarapu, P. R.; Sharma, N.; Peterson, V.; Adams, S. Variation in Structure and Li^+-Ion Migration in Argyrodite-type Li_6PS_5X (X = Cl, Br, I) Solid Electrolytes. *J. Solid State Chem.* **2011**, *16*, 1807-1813.

(36) Yu, C.; Ganapathy, S.; Hageman, J.; van Eijck, L.; van Eck, E. R.; Zhang, L.; Schwietert, T.; Basak, S.; Kelder, E. M.; Wagemaker, M. Facile Synthesis toward the Optimal Structure-Conductivity Characteristics of the Argyrodite Li_6PS_5Cl Solid-State Electrolyte. *ACS Appl. Mater. Interfaces* **2018**, *10*, 33296-33306.

(37) Zhou, L.; Park, K. H.; Sun, X.; Lalère, F.; Adermann, T.; Hartmann, P.; Nazar, L. F. Solvent-Engineered Design of Argyrodite Li_6PS_5X (X = Cl, Br, I) Solid Electrolytes with High Ionic Conductivity. *ACS Energy Lett.* **2019**, *4*, 265-270.

(38) De Klerk, N. J.; Rosłoń, I.; Wagemaker, M. Diffusion Mechanism of Li Argyrodite Solid Electrolytes for Li-Ion Batteries and Prediction of Optimized Halogen Doping: The Effect of Li Vacancies, Halogens, and Halogen Disorder. *Chem. Mater.* **2016**, *28*, 7955-7963.

(39) Kuhn, A.; Duppel, V.; Lotsch, B. V. Tetragonal $Li_{10}GeP_2S_{12}$ and Li_7GePS_8 - Exploring the Li Ion Dynamics in LGPS Li Electrolytes. *Energy Environ. Sci.* **2013**, *6*, 3548-3552.

(40) Xu, R.; Wu, Z.; Zhang, S.; Wang, X.; Xia, Y.; Xia, X.; Huang, X.; Tu, J. Construction of All-Solid-State Batteries based on a Sulfur-Graphene Composite and $Li_{9.54}Si_{1.74}P_{1.44}S_{11.7}Cl_{0.3}$ Solid Electrolyte. *Chem.: Eur. J* **2017**, *23*, 13950-13956.

(41) Wu, F.; Fitzhugh, W.; Ye, L.; Ning, J.; Li, X. Advanced Sulfide Solid Electrolyte by Core-Shell Structural Design. *Nat. Commun.* **2018**, *9*, 4037.

(42) Kraft, M. A.; Culver, S. P.; Calderon, M.; Böcher, F.; Krauskopf, T.; Senyshyn, A.; Dietrich, C.; Zevalkink, A.; Janek, J.; Zeier, W. G. Influence of Lattice Polarizability on the Ionic Conductivity in the Lithium Superionic Argyrodites Li_6PS_5X (X = Cl, Br, I). *J. Am. Chem. Soc.* **2017**, *139*, 10909−10918.

(43) Ohno, S.; Helm, B.; Fuchs, T.; Dewald, G.; Kraft, M. A.; Culver, S. P.; Senyshyn, A.; Zeier, W. G. Further Evidence for Energy Landscape Flattening in the Superionic Argyrodites $Li_{6+x}P_{1-x}M_xS_5I$ (M = Si, Ge, Sn). *Chem. Mater.* **2019**, *31*, 4936-4944.

(44) Rietveld, H. M. A Profile Refinement Method for Nuclear and Magnetic Structures. *J. Appl. Cryst.* **1969**, *2*, 65-71.

(45) Toby, B. H.; Von Dreele, R. B. GSAS-II: the Genesis of a Modern Open-Source All Purpose Crystallography Software Package. *J. Appl. Crystallogr.* **2013**, *46*, 544-549.

(46) Chen, H.; Wong, L. L.; Adams, S. SoftBV - a Software Tool for Screening the Materials Genome of Inorganic Fast Ion Conductors. *Acta Crystallogr., Sect. B: Struct. Sci., Cryst. Eng. Mater.* **2019**, *75*, 18-33.

(47) Dawson, J. A.; Canepa, P.; Famprikis, T.; Masquelier, C.; Islam, M. S. Atomic-Scale Influence of Grain Boundaries on Li-Ion Conduction in Solid Electrolytes for All-Solid-State Batteries. *J. Am. Chem. Soc.* **2017**, *140*, 362-368.

(48) Ganapathy, S.; Yu, C.; van Eck, E. R. H.; Wagemaker, M. Peeking across Grain Boundaries in a Solid-State Ionic Conductor. *ACS Energy Lett.* **2019**, *4*, 1092-1097.

(49) Gorochov, O. Compounds Ag_8MX_6 (M=Si Ge Sn and X=S Se Te). *Bull. Soc. Chim. Fr.* **1968**, *6*, 2263.

(50) Alverdiyev, I. J.; Aliev, Z. S.; Bagheri, S. M.; Mashadiyeva, L. F.; Yusibov, Y. A.; Babanly, M. B. Study of the $2Cu_2S + GeSe_2 \leftrightarrow 2Cu_2Se + GeS_2$ reciprocal system and thermodynamic properties of the $Cu_8GeS_{6-x}Se_x$ solid solutions. *J. Alloys Compd.* **2017**, *691*, 255-262.

(51) Yu, C.; Ganapathy, S.; de Klerk, N. J. J.; Roslon, I.; van Eck, E. R. H.; Kentgens, A. P. M.; Wagemaker, M. Unravelling Li-Ion Transport from Picoseconds to Seconds: Bulk versus Interfaces in an Argyrodite Li_6PS_5Cl-Li_2S All-Solid-State Li-Ion Battery. *J. Am. Chem. Soc.* **2016**, *138*, 11192-11201.

(52) Gao, Y.; Wang, D.; Li, Y. C.; Yu, Z.; Mallouk, T. E.; Wang, D. Salt-Based Organic-Inorganic Nanocomposites: Towards A Stable Lithium Metal/$Li_{10}GeP_2S_{12}$ Solid Electrolyte Interface. *Angew. Chem. Int. Ed.* **2018**, *57*, 13608-13612.

(53) Wenzel, S.; Randau, S.; Leichtweiß, T,; Weber, D. A.; Sann, J.; Zeier, W. G.; Janek, J. Direct Observation of the Interfacial Instability of the Fast Ionic Conductor $Li_{10}GeP_2S_{12}$ at the Lithium Metal Anode. *Chem. Mater.* **2016**, *28*, 2400-2407.

(54) Kasemchainan, J.; Zekoll, S.; Jolly, D. S.; Ning, Z.; Hartley, G. O.; Marrow, J.; Bruce, P. G. Critical Stripping Current Leads to Dendrite Formation on Plating in Lithium Anode Solid Electrolyte Cells. *Nat. Mater.* **2019**, *18*, 1105-1111.

(55) Krauskopf, T.; Dippel, R.; Hartmann, H.; Peppler, K.; Mogwitz, B.; Richter, F. H.; Zeier, W. G.; Janek, J. Lithium-Metal Growth Kinetics on LLZO Garnet-Type Solid Electrolytes. *Joule* **2019**, *3*, 2030-2049.

(56) He, X.; Zhu, Y.; Mo, Y. Origin of Fast Ion Diffusion in Super-Ionic Conductors. *Nat. Commun.* **2017**, *8*, 15893.

(57) Wang, Y.; Richards, W. D.; Ong, S. P.; Miara, L. J.; Kim, J. C.; Mo, Y.; Ceder, G. Design Principles for Solid-State Lithium Superionic Conductors. *Nat. Mater.* **2015**, *14*, 1026, 1031.

(58) Zhou, L.; Assoud, A.; Shamsunder, A.; Huq, A.; Zhang, Q.; Hartmann, P.; Kulisch, J.; Nazar, L. F. An Entropically Stabilized Fast-Ion Conductor: $Li_{3.25}[Si_{0.25}P_{0.75}]S_4$. *Chem. Mater.* **2019**, *31*, 7801-7811.

(59) Duevel, A. Heitjans, P.; Pedorov, P.; Scholz, G.; Cibin, G.; Chadwick, A. V.; Pickup, D.; Ramos, S.; Sayle, L. W. L.; Sayle, E. K. L.; Sayle, T. X. T.; Sayle, D. C. Is Geometric Frustration-Induced Disorder a Recipe for High Ionic Conductivity? *J. Am. Chem. Soc.* **2017**, *139*, 5842 - 5848.

(60) Kweon, K. E.; Varley, J. B.; Shea, P.; Adelstein, N.; Mehta, P.; Heo, T. W.; Udovic, T. J.;Stavila, V.; Wood, B. C. Structural, Chemical, and Dynamical Frustration: Origins of Superionic Conductivity in *closo*-Borate Solid Electrolytes. *Chem. Mater.* **2017**, *29*, 9142-9153.

(61) Deng, Y.; Eames, C.; Chotard, J.; Lalere, F.; Seznec, V.; Emge, S.; Pecher, O.; Grey, C. P.; Masquelier, C.; Islam, M. S. Structural and Mechanistic Insights into Fast Lithium-Ion Conduction in Li_4SiO_4-Li_3PO_4 Solid Electrolytes. *J. Am. Chem. Soc.* **2015**, *137*, 9136-9145.

(62) Samson, A. J.; Hofstetter, K.; Bag, S.; Thangadurai, V. A Bird's-eye View of Li-Stuffed Garnet-type $Li_7La_3Zr_2O_{12}$ Ceramic Electrolytes for Advanced All-Solid-State Li Batteries. *Energy Environ. Sci.* **2019**, 10.1039/C9EE01548E.

(63) He, X.; Bai, Q.; Liu, Y.; Nolan, A.M.; Ling, C.; Mo, Y. Crystal Structural Framework of Lithium Super-Ionic Conductors. *Adv. Energy Mater*. 2019, doi.org/10.1002/aenm.201902078

TOC